# Carbon-loaded flexible electrode films for Li-$O_2$ cells: Preparation, Porosity, Homogeneity and Electrochemical characterization

*Caroline Gaya[a,b,c], Alejandro A. Franco [b,c,d,e], Christine Surcin [b,c], Matthieu Courty [b,c] and Dominique Larcher [b,c,d,*]*

[a] *IRT Saint Exupéry, 3 rue Tarfaya, Cedex 34436, Toulouse Cedex 4, France*
[b] *Laboratoire de Réactivité et Chimie des Solides (LRCS), CNRS UMR 7314, Université de Picardie Jules Verne, 33 rue St Leu, 80039 Amiens Cedex, France*
[c] *Réseau sur le Stockage Electrochimique de l'Energie (RS2E), FR CNRS 3459, 33 rue Saint Leu, 80039 Amiens Cedex, France*
[d] ALISTORE European Research Institute, FR CNRS 3104, 33 rue Saint Leu, 80039 Amiens Cedex, France
[e] *Institut Universitaire de France, 103 Boulevard Saint-Michel, 75005 Paris Cedex, France*

* Corresponding author: Dominique Larcher (dominique.larcher@u-picardie.fr)

**ABSTRACT**

Porous (up to 70 vol. %) self-standing flexible carbon/polymer (Ketjen Black / PVdF-HFP) film electrodes are produced by leaching out a plasticizer-porogen agent (DBP = DiButyl Phtalate) from precursor films (80% ≥ DBP w% ≥ 40%). Textural analysis reveals that i) these films exhibit copious initial macroporosity, ii) extra open macro- and then meso-porosity are created along the leaching, iii) this leaching process impacts the internal films texture resulting in a partial closing of the pre-existing porosity, iv) only films with the lowest initial DBP contents (≤ 60 w%) are homogeneous in composition/porosity/texture. In Li/$O_2$ cells, the first discharge capacities of these films are compared to those calculated assuming a total filling of this porosity by electrochemically formed solid $Li_2O_2$ (2700 mAh.cm$^{-3}$ of pores). Up to 80 % of the maximum capacity can be reached (i.e. 80 % of the porosity filled by $Li_2O_2$), confirming the positive attributes of mixed interconnected macro/meso porosity. This is further emphasized by the very low capacities obtained with electrodes having similar porosity vol. % but totally different internal texture (GDL). These conclusions can be made despite a large discrepancy in the data, even for homogeneous films, due to reproducibility issues intrinsic to the system.

**Keywords:** Li-$O_2$ battery, air electrode, carbon/polymer electrodes, porogen, porosity,

**Highlights:**

- Flexible highly porous C-loaded electrodes are easily produced by porogen leaching
- These films hold a porous network made of interconnected open macro- and meso-pores
- Only films with initial porogen (DBP) contents lower than 60 w% are homogeneous
- As cathode in Li/$O_2$ cells, most of this mixed porosity can be filled by $Li_2O_2$
- Such multi-porous architecture is thus promoting high capacity for Li/$O_2$ cells

## INTRODUCTION

Mastering the electrode texture (specific surface area, porosity, tortuosity, pore size distribution) is of paramount importance in the field of electrochemical energy conversion and storage. For Li-ion and next generation (e.g. Na-ion) batteries, the characteristics of the electrodes porosity strongly drives the characteristics of the electronic and ionic percolation networks which consequently drastically impacts the power vs. energy densities of the cells. Also, in supercapacitors using carbon-based electrodes, it was shown that micro-pores with diameter in the (sub)nanometer range, *i.e.* smaller than solvated electrolyte ions, can host bare (de-solvated) ions hence increasing largely the surface capacitance of the electrode.[1] In PEMFC (Proton Exchange Membrane Fuel Cell), the reduction of oxygen into water at the cathode takes place at the surface of Pt nanoparticles supported either at the surface of carbon particles or inside their inner pores. The electrode texture impacts the transport of the formed water[2] and consequently the ORR kinetics and carbon corrosion mechanisms.[3]

Aside from these mature technologies, several options under exploration in the field, like metal-air and Li-sulfur batteries, require the use of specifically designed electrodes with architecture enabling optimum operation [4,5]. Regarding Li-air systems, numerous modeling and theoretical works have been recently devoted to the prediction of the optimum electrode architecture enabling the maximum accessibility of the reactants (dissolved $Li^+$ and $O_2$) to the electrode conducting surface (generally carbons), hence the maximum capacity resulting from the electrochemical formation of $Li_2O_2$ ($2Li^+ + 2e^- + O_2 \rightarrow Li_2O_2$).[6] In contrast, only a few works combine the experimental characterization of the electrodes texture/porosity and their electrochemical performances.[7,8] Anyway, from both aspects, a mixture of macro- and meso-porosity in the conducting electrode is considered as necessary to ensure good reactivity and acceptable capacity. This rises now the question: how can we easily and reproducibly prepare such carbon-based bi-porous electrodes?

The controlled removal of a volatile solvent from a liquid slurry is a common way to reproducibly produce porosity at the industrial scale, but the elimination of a porogenic substance from a solid matrix is another appealing templating option. As an example, the dissolution by water of embedded NaCl grains having controlled size leads to well-defined open porosity as applied to metallic foams[9] or thick binder-free composite electrodes for Li-ion batteries with enhanced performances.[10] Worth pointing out that such dissolution-driven process potentially ensures that the created porosity is then fully accessible to liquid (electrolyte). The same approach can be applied to plastic films from which an organic porogen agent is removed by dissolution thanks to an appropriate solvent. This is the bottom line of the so-called Bellcore technology, which led to the development of the first practical plastic electrodes [11] allowing the production of a full plastic (solid-liquid hybrid) Li-ion battery (PLion) [12–15] with high performances.[16–18] This process produces freestanding electrodes [16,19]

with high flexibility, good mechanical properties [11,15,20,21], easy to process and to upscale at the industrial level.[11,15] It consists of three steps:

1) the production of a flexible plastic film containing the electro-active material, a conducting additive (divided carbon), a porogen / plasticizer substance (DBP = DiButyl Phtalate, *ca.* 25 w%), and a polymeric binder (PVdF-HFP) playing the role of a matrix maintaining the whole together;
2) the creation of porosity by leaching DBP out of the film by soaked in ether;
3) the filling of the as-created porosity by the battery liquid electrolyte by simply dipping in it the porous film electrode [15,17].

The crystalline parts of the plastic binder ensure mechanical stability of the electrode while its amorphous domains help in trapping the electrolyte. Highly volatile solvents, such as ether, are used to remove the porogen agent. This removal step can be performed at room temperature, creating porosity which will later be accessible to the electrolyte (pore memory). Garza et *al.* mentioned that several washing steps are requested [22] while Tarascon et *al.* specified that the volume of absorbed electrolyte is lower than the initial volume of DBP in the electrode formulation.[11] Also, such electrode technology can help to get deeper insights on batteries active materials behavior as it can be applied to many materials [23–29], and often facilitates *in situ* measurements (*e.g.* XRD, Mössbauer, EXAFS). [21,29,30]

The importance of the binder was far more scrutinized [31–33] than that of the porogen agent. Different ways of improving the fabrication process have been considered such as changing the solvent and using mix of acetone/ethanol, acrylonitrile or acetonitrile[31,33,34] or changing the polymeric binder.[31,33,35] In addition, propylene carbonate and ethylene carbonate / propylene carbonate mixes have been considered instead of DBP as porogen substance.[17,22,29] Du Pasquier et *al.* suggested to bypass the extraction step thanks to the modification of the PVdF-HFP polymer.[15]

In this paper, we will describe the preparation and characterization of highly porous carbon-loaded flexible films, focusing on high initial DBP contents (80% $\geq$ DBP w% $\geq$ 40%). We will thoroughly analyze the texture of the films (specific surface area, porous volume, open porosity, macro- vs. meso-porosity …) before and during the leaching process, as well as its homogeneity. As we target Li-$O_2$ applications, we maximized the accessible specific surface area by using highly divided carbon as active material. Then, experimental first discharge capacities will be compared to the theoretical ones evaluated from textural data of the films. By the way, this will be a good opportunity for us to express electrode capacities relatively to that maximum theoretically achievable (%) based on the porosity. This is probably one of the most convenient way to compare and rationalize data related to such electrodes hosting the solid product of an electrochemical reaction.

## EXPERIMENTAL

*Making and Characterization of the electrodes*

Due to the use of such highly divided carbon (Ketjen Black, EC600-JD, Akzo Nobel, 1400 $m^2.g^{-1}$), the electrode formulation had to be accordingly adapted. In particular, the polymer binder (PVdF-HFP, Kynar Flex 2801, Arkema) content (w%) had to be modified in order to produce self-standing and flexible films, and we found that a 4/1 (polymer/C) weight ratio is necessary for that, and it will be kept constant all along the present study.

Weighted amounts of powders (carbon + polymer) were mixed in a mortar. Then, liquid DBP (Acros Organic, 99% purity, density: 1.05) and acetone (acting as solvent) were successively added to the powder mixture and the resulting slurry was magnetically stirred in a closed container for 90 minutes. Eventually, the amount of acetone was adapted to produce slurries with equivalent apparent viscosities and so behaving alike during the casting step. The dry mass ratio, i.e. the amount of solids (C+polymer) compared to the overall mass of the slurry, was then kept in a similar range (11 to 16 w%). Densities and BET specific surface area values of the electrode components are summarized in **Table 1**, and **Table 2** sums up the ratios used in the different formulations, with DBP / solids ratio ranging from 40 to 80 w%.

| Components | Density ($g.cm^{-3}$) | BET specific surface area ($m^2.g^{-1}$) |
|---|---|---|
| Ketjen Black | 2.23 | 1400 |
| PVdF-HFP | 1.79 | 7.5 |
| DBP | 1.05 | / |

***Table 1**: Characteristics of the electrode components*

| **DBP (w%)** | 40 | 61 | 65 | 80 |
|---|---|---|---|---|
| **Carbon (w%)** | 13 | 8 | 7 | 4 |
| **Polymer (w%)** | 47 | 31 | 28 | 16 |
| **Dry mass (%)** | 16 | 14 | 15 | 11 |

***Table 2**: Weight ratios of the several components of the slurries*

While DBP amount was increased, acetone ratio was modulated, as illustrated in **Table 3**, to ensure analogous liquid/solid volume ratios. Each slurry was then casted at constant speed on a Mylar foil using an automatic doctor blading (Elcometer 4340) with a gap of 400 µm and the resulting films were dried at ambient temperature. Films were named from their DBP w%, and referred to as $DBP_{w\%}$. Once acetone is fully evaporated and the film formed,

electrodes were cut into disks (Ø : 11 mm) and DBP was extracted thanks to 3 consecutives treatments in ether (VWR Chemicals, GPR RectaPur) of 15 minutes each.

| **Carbon (v%)** | 1 | 1 | 1 | 1 |
|---|---|---|---|---|
| **Polymer (v%)** | 5 | 5 | 5 | 4 |
| **DBP (v%)** | 8 | 16 | 21 | 37 |
| **Acetone (v%)** | 86 | 78 | 72 | 58 |
| ***Liquids (v%)*** | *94* | *94* | *94* | *95* |

***Table 3****: Volume ratios of the several components of the slurries and % volume of liquids (DBP+acetone)*

Eventually, films flatness was ensured by squeezing them between two glass slides along the ether removal. The apparent volume of selected disks/films was calculated from their measured diameters and thicknesses, before and after DBP extraction. Films and electrodes thicknesses were evaluated thanks to a digital Vernier caliper (± 1 μm). Each sample was placed between two glass slides to limit compression of the film during measurements. The overall thickness was measured repetitively and the mean value considered for calculations. Punctually, thickness was also checked by direct SEM imaging.

Before, during and after DBP extraction, films were also analyzed for their density by helium pycnometry (AccuPyc 1330, Micromeritics), as well as for their meso-porosity (BJH formalism[36]) and specific surface areas (SSA, BET formalism[37]) by $N_2$ adsorption at 77 K (ASAP 2020, Micromeritics). Worth pointing out that macro-porosity (pore radius > 50 nm) is not measured in our experimental conditions, but all the surfaces will be accessed, probed and measured regardless of the pores size. Prior to analysis, each sample is degassed by heating under vacuum (30 μm Hg). Here, extreme caution has to be exercised in setting the temperature to avoid vaporization/loss of DBP and melting of the plastic matrix. Preliminary tests performed at 150 °C revealed the formation of colorless droplets inside the sample tube during degassing of not-extracted (*i.e.* DBP containing) films. This liquid was easily identified by infrared spectroscopy as pure DBP, i.e. extracted from the films, in agreement with a vapor pressure (~1 mm Hg) largely overpassing the applied pressure (30 mm Hg) at this temperature.[38] By the way, at industrial level, this may constitute an easier method to implement compared to manipulating volatile solvents.[39] To avoid this phenomenon, the temperature should be set below 100°C. Regarding the plastic stability, thermal analysis (DSC) revealed that the onset for its melting is around 110°C. So, the degassing was systematically performed at 95°C.

Alternatively, gas diffusion layer (GDL, H23, Freudenberg) carbon electrodes were also used as cathode. It consists of thin disks made of interlaced long carbon fibers having around 10 μm in diameter (**Figure 3-d**).

*Cells making, flushing, cycling*

The electrochemical cells were assembled in dry Ar-filled glovebox. The cells were based on classical Swagelok design, except the top current collector piston was made of a hollow stainless tube to let oxygen accessing the cathode. Before being transferred in the glovebox, the Swagelok elements were dried two hours at 70 °C. From the bottom to the top were stacked a lithium disk (Ø = 9 mm), two disks of glassfibers (Whatman, Ø = 14 mm), the cathode flexible film (Ø = 9 mm) and finally a stainless steel grid (Ø = 11 mm). Then, the stack was soaked with 325 µL of electrolyte (0.5 M LiTFSI in TriGDME, Acros Organic). Once the hollow top plunger screwed, the cells were inserted in a tight glass container enabling electronic contacts and control of the atmosphere. Within the container, the cells were flushed with pure oxygen (1.5 $L.h^{-1}$) for thirty minutes and then discharged using a VSP (Bio-Logic) cycler. Cycling was performed at 20°C, between 2 and 3 Volts vs $Li^+/Li°$, at constant 50 µA current.

**RESULTS**

*Films porosity and homogeneity*

The efficiency of the DBP removal was estimated by a statistical study carried out on 50 disks cut from $DBP_{65}$. Each disk was weighted before and after full leaching process (3 consecutive soakings in pure ether) and the resulting weight loss was then compared to the initial mass of DBP in the disk, leading to the efficiency of the removal (%) **(Figure 1)**.

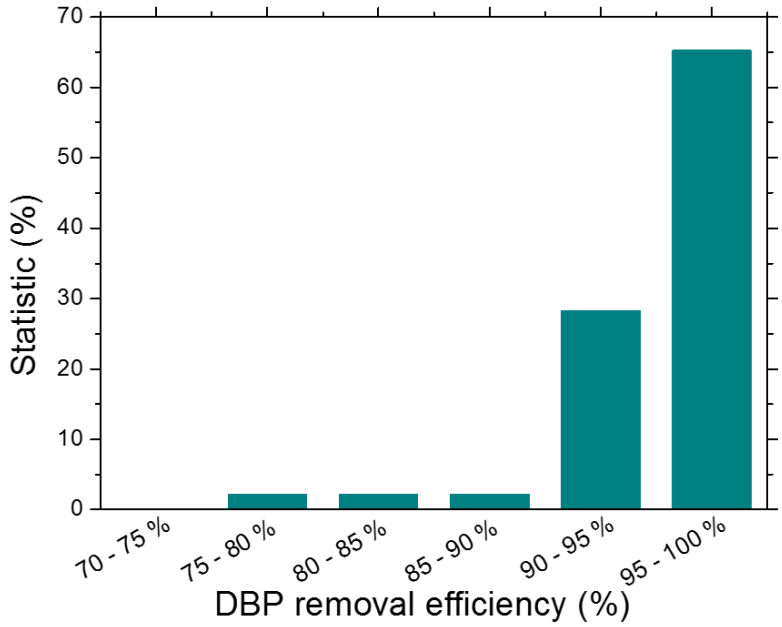


***Figure 1**: Statistical analysis of the efficiency of the DBP extraction (50 disks from $DBP_{65}$)*

The mean leaching efficiency was found equal to 94.4 %. DBP extraction was in the 90 - 100 % efficiency range for 94 % of the disks, and there is no disk with an extraction efficiency lower than 75 %. Although these results could mean that the DBP removal is, statistically, almost fully accomplished for electrode films with such high DBP contents, their punctual slight deviation from full (100 % efficient) leaching can also enlighten some inhomogeneity in the DBP content through the entire films from which the disks were cut. This is of paramount importance since the initial chemical inhomogeneity will straightly impact the texture of the DBP-extracted electrode films.

Thus, in order to get more accurate data on the textural evolution of these films, we decided to compare the behavior of 3 films having very different DBP initial contents, namely $DBP_{40}$, $DBP_{60}$ and $DBP_{80}$.

Based on the weight composition **(Table 2)** and individual density of the components **(Table 1)**, we can easily calculate the expected initial (C-polymer-DBP) and final (C-polymer) densities of the films. Whereas the initial density is bound to the DBP films content, that of the extracted films is theoretically constant ($\rho$=1.88 $cm^3.g^{-1}$) since only made of polymer ($\rho$=1.79 $cm^3.g^{-1}$) and C ($\rho$=2.23 $cm^3.g^{-1}$) in the same weight ratio (4/1). Pycnometer measurements performed on large (tens of $cm^2$) stripes of films led to density values in very good agreement with the expected ones **(Table 4)**. Not only this confirms the chemical composition of the films and the juxtaposition of their components, but much more importantly demonstrates the absence of significant closed porosity (*i.e.* inaccessible to He) in our DBP-rich films. Indeed, such closed porosity could have been expected from fast acetone evaporation steps.

| | With DBP | | | DBP extracted | |
|---|---|---|---|---|---|
| | **Initial density ($g.cm^{-3}$) Calcul. / Meas.** | **Mesoporous Volume (ASAP, v%)** | **BET SSA ($m^2.g^{-1}$)** | **Mesoporous Volume (ASAP, v%)** | **BET SSA ($m^2.g^{-1}$)** |
| $DBP_{40}$ | 1.42 / 1.38 | ~0 | | 10 | 31.7 |
| $DBP_{60}$ | 1.27 / 1.32 | | 2.5 | 14 | 56.2 |
| $DBP_{80}$ | 1.15 / …. | | | 12 | 33.0 |

***Table 4**: Textural characterization of $DBP_{40}$, $DBP_{60}$ and $DBP_{80}$ films before and after DBP leaching*

Once discarded the possibility of an initial closed porosity, we evaluated the total initial porosity (porous v%, blue bars in **Figure 2**) of our films by simply comparing their apparent volumes (thickness x surface area) with the sum of that of their components (C+polymer+DBP). Three disks were cut from $DBP_{40}$, and their porous volumes were found ranging from 44 to 49 v%, clueing a very good homogeneity of the film. Furthermore, based on previous density analyses, this high initial porosity is obviously open and accessible. Also, nitrogen adsorption analyses showing negligible meso-porous contribution (0.002 $cm^3.g^{-1}$) and

very low SSA (2.5 $m^2.g^{-1}$), this high initial porosity is due to macro-pores. Moving towards higher DBP contents, similar analyses demonstrate that the films are getting more and more heterogeneous. Indeed, porous volumes are found ranging from 33 % to 42 % for $DBP_{60}$, and from 0 % to 42 % for $DBP_{80}$ (blue bars in **Figure 2**).

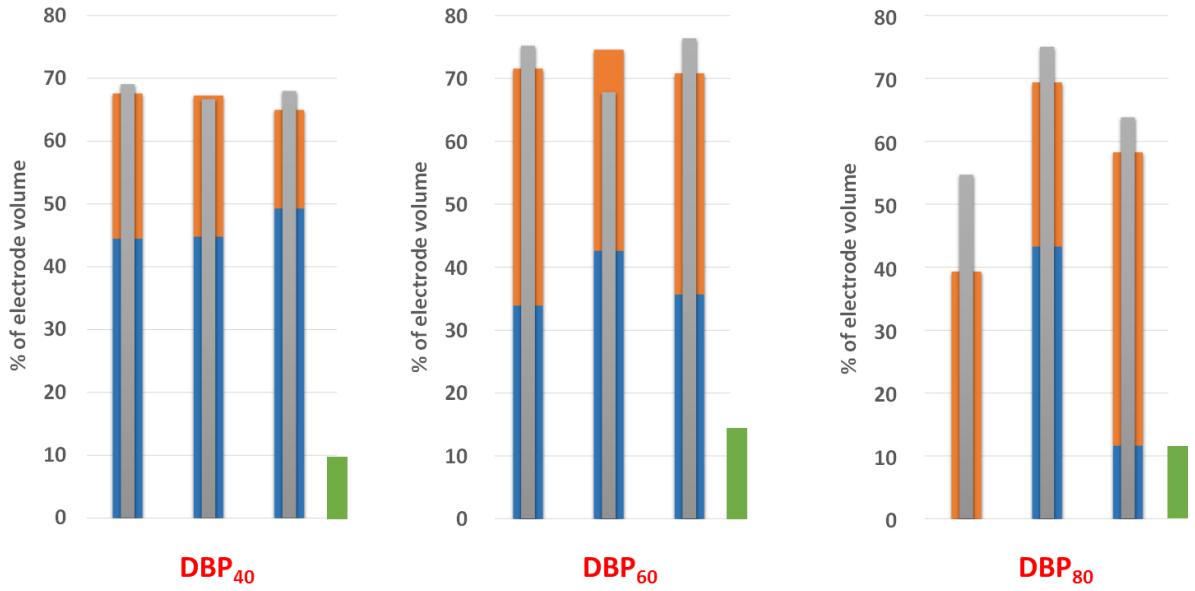


***Figure 2**: Total porosity (volume %) for three disks cut from $DBP_{40}$, $DBP_{60}$ and $DBP_{80}$ films, measured before (blue bars) and after (gray bars) DBP extraction.*
*The orange bars represent the volume of DBP extracted during the ether leaching.*
*The green bars represent the mesoporous contribution to the total volume of extracted films.*

The total porosities of the disks were similarly evaluated after DBP extraction (gray bars on **Figure 2**). As expected, the global porosity is found systematically increased by the DBP extraction, but the heterogeneity trend previously spotted for the initial porous volumes is here similarly observed for the final porosities (67-69 v% for $DBP_{40}$, 68-77 v% for $DBP_{60}$, and 54-74 v% for $DBP_{80}$). Higher the initial DBP content, higher the discrepancy in both the initial and final porous volumes throughout the casted films.

Knowing the density of DBP (1.05 $g.cm^{-3}$) and assuming that the evolution in the film weight during ether extraction is only due to the DBP dissolution, we can easily estimate the porous volume left behind based on the experimental film mass loss. These v% values are shown as orange bars in **Figure 2**. For the 3 disks cut from $DBP_{40}$, we can clearly see that this calculated DBP-related porous volume satisfyingly matches the gap between the initial and final global porosity. This match is less pronounced for $DBP_{60}$ and even worst for $DBP_{80}$. Again, this nicely illustrates the large heterogeneity in the films composition and texture for the highest initial DBP contents.

For electrochemical applications, quantitative knowledge on the global porosity is not sufficient. Accessibility and pore size also matter. In order to get more insight on these aspects, BET SSA and meso-porous volume where determined by $N_2$ isotherm adsorption (**Table 4**). As exemplified by $DBP_{60}$, DBP extraction clearly provokes / triggers the creation of open and

accessible meso-pores, totally absent in the precursor films, but not proportionally with the initial DBP content (**Table 4,** green bars on **Figure 2**). Since meso-pores have high surface/volume ratio, this logically comes with a large increase in SSA (**Table 4**). Whatever the initial DBP content, meso-porous volume (green bars on **Figure 2**) is always lower than the volume of extracted DBP, meaning that this extraction also creates some macro-porosity.

Pycnometry analyses of extracted films reveal density values spreading from 1.37 ($DBP_{40}$) to 1.65 $g.cm^{-3}$ ($DBP_{60}$), which is very much lower than expected (1.88 $g.cm^{-3}$). The only way to explain this surprising result is a significant evolution of the internal film texture during DBP leaching and/or drying step, resulting in the closing (*i.e.* not any more accessible to He) of a part of the initial or created porosity. As a quantitative example, the difference between expected and measured density for extracted $DBP_{40}$ and $DBP_{60}$ films corresponds to a final electrode having ca. 25 % of its volume made of not accessible porosity. This internal reorganization is probably at the origin of the shape evolution and curling of the disks we observed during the DBP extraction and drying steps (slight decrease in thickness, slight increase in diameter). Note that these changes do not result in significant overall volume evolution of the disks/films, making us confident in our textural survey and conclusions. This reorganization can also shade some light on the low efficiency of the DBP removal spotted for $DBP_{80}$ film that never exceeds 60 %, some DBP remaining trapped in isolated inner parts of the film and not accessible to ether percolation.

SEM pictures of films before and after DBP extraction **(Figure 3)** confirm the textural effect of the DBP content before and after the leaching steps. Clearly, non-extracted films exhibit increasing surface roughness and larger micrometric voids/cracks with increasing initial DBP content. Extracted films exhibit further voids and pores, delimiting C/polymer agglomerates, especially for $DBP_{60}$, and $DBP_{80}$.

Let's now explore the individual impact of each of the three ether treatments. Both the porous volume and SSA neatly increase during each leaching step while DBP is progressively extracted (**Table 5**).

| Cleaning step | Total DBP loss (%) | ASAP (meso)porous volume ($cm^3.g^{-1}$) | BET specific surface area (SSA, $m^2.g^{-1}$) |
|---|---|---|---|
| #0 | - | 0.002 | 2.5 |
| #1 | 69 | 0.053 | 7.2 |
| #2 | 97 | 0.133 | 25.7 |
| #3 | 97.4 | 0.243 | 56.2 |

***Table 5**: Evolutions in weight loss, porous volume and BET specific surface area (SSA) for $DBP_{60}$ along DBP extraction steps.*

Even though resulting in a very slim DBP loss (0.4 %), step#3 is associated with the largest porous volume and SSA increases, clearly confirming the need of the three steps. The slight amount (<3%) of remaining non-dissolved DBP is likely located in isolated inner parts of

the film, non-accessible to ether percolation. Note that the maximum films SSA remains lower (56 $m^2.g^{-1}$) than the Ketjen Black expected contribution (280 $m^2.g^{-1}$ for $DBP_{60}$), confirming that carbon particles are embedded in the polymeric film, hindering a part of its surface. Yet, a significant amount of the carbon surface is accessible. Because large (macro)pores have small surface/volume ratio, the slight increase in SSA spotted during step #1 (2.5 → 7.2 $m^2.g^{-1}$), while more than two third (69%) of the DBP was gone, indicates the formation of large (macro) pores from easily accessible large DBP-rich zones of the films, therefore firstly and quickly extracted. Thereafter, smaller and less accessible DBP clusters are progressively accessed and leached out along the subsequent two steps (#2 and #3). This explains the much larger gains in SSA, especially during step#3. We logically believe this is taking place within the micrometric C/binder agglomerates clearly visible on the SEM images, and between which, large micrometric macro-pores are also clearly observed (**Figure 3**).

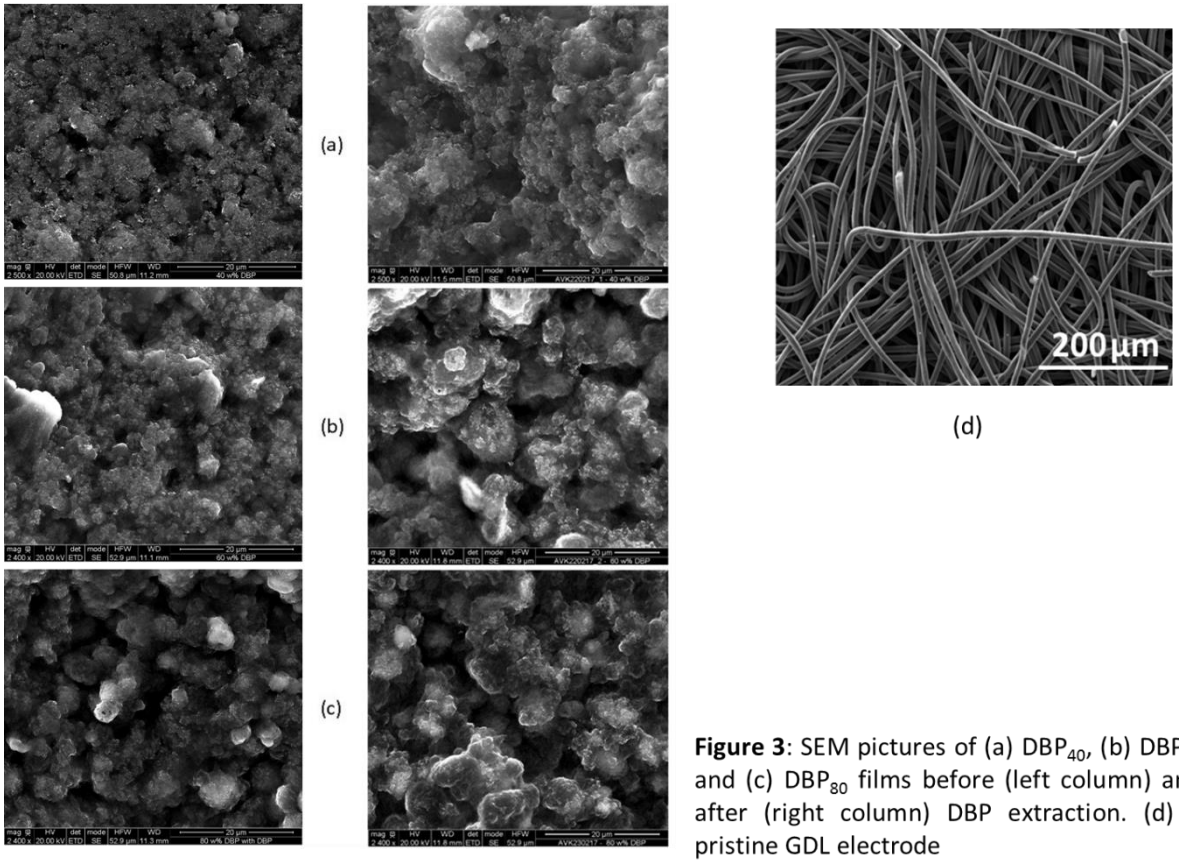


**Figure 3**: SEM pictures of (a) $DBP_{40}$, (b) $DBP_{60}$ and (c) $DBP_{80}$ films before (left column) and after (right column) DBP extraction. (d) a pristine GDL electrode

The ratio between the gain in porous volume and the gain in SSA gives a first evaluation of the related pore size, and we found it is lying below 10 nm during steps #2 and #3. Attempts to replace the 3 leaching steps (of 15 min each) by a unique one lasting 45 minutes systematically resulted is a lower porous volume, likely clueing some kinetics and/or saturation issues in DBP-containing ether.

*Electrochemical response of the films in Li/$O_2$ configuration*

**Figure 4** compares the first galvanostatic discharges for GDL electrodes and for extracted disks cut from $DBP_{60}$ film, both set having equivalent total porosity. Clearly, $DBP_{60}$ electrodes allow to reach much higher gravimetric capacities (mAh.$g^{-1}$) than GDL, despite the recurrent very bad reproducibility of the data. Capacities of $DBP_{60}$ electrodes range from 200 to 2600 mAh.$g^{-1}$, those of GDL range from 2 to 87 mAh.$g^{-1}$. From the porosity data gathered on our electrodes, we can estimate what should be their maximum capacity in Li/$O_2$ cells, assuming that it corresponds to the total filling of the porosity by electrochemically formed $Li_2O_2$ solid ($\rho$ = 2.3 g.$cm^{-3}$). Our data show that up to 80 % of the maximum capacity can be reached for $DBP_{60}$ electrodes, while less than 3 % is spotted for GDL.

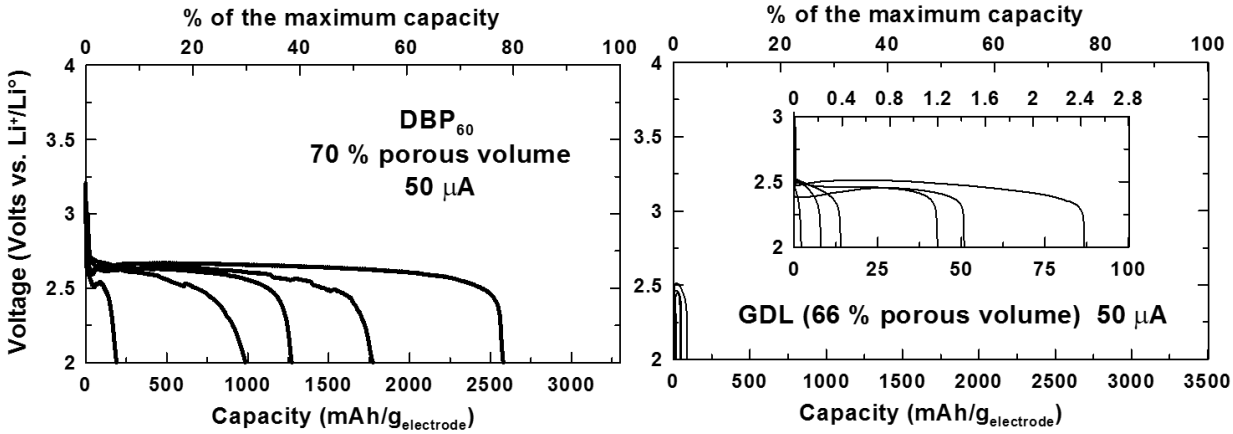


***Figure 4**: First galvanostatic (i = 50 μA) discharge curves in Li/$O_2$ cell configuration for $DBP_{60}$ electrodes (left panel) and GDL electrodes (right panel). Inset in right panel is an enlargement of the main plot. Cells were cycled in static pure $O_2$, at T = 20°C.*

## CONCLUSIONS

Texture of highly porous-carbon loaded plastic films, initially containing DBP contents ranging from 40 to 80 w%, were qualitatively and quantitatively evaluated before and along the DBP removing process. All non-extracted films exhibit copious open and accessible macroporosity (as high as 40 v%) and no meso-pores. DBP extraction triggers the formation of significant extra meso- and macro-porosity, but also provokes an internal reorganization leading to the closing of a part of the film porosity. Even though a statistical study reveals an apparent high efficiency of the DBP extraction (*e.g.* 94 % of the samples cut from $DBP_{65}$ films reached between 90 to 100 % of extraction efficiency), other results clearly show that higher is the initial DBP content, more pronounced is the chemical inhomogeneity throughout the films. This is a main drawback as it will radically impact the local textural properties of the film, such as the initial and final porosities. Nevertheless, $DBP_{40}$ and $DBP_{60}$ films display an initial homogeneous open macro-porosity and composition, resulting in a similar homogeneity after extraction. The first DBP extraction step was found to mainly generate macro-porosity, while the two last steps generate the meso-porosity, hence emphasizing the necessity of the three steps. Electrochemical performances of $DBP_{60}$ electrodes were compared with those of carbon GDL electrodes. Both have equivalent total internal porosity (66-70 v%) but GDL is only macroporous (micron-size pores) while $DBP_{60}$ has multi-size interconnected pores ranging from micron-size to meso-pores. Despite an intrinsic and recurrent lack of reproducibility [40], $Li/O_2$ cell tests clearly demonstrate that interconnected multi-size porosity ($DBP_{60}$) enables much larger capacities than macro-porosity (GDL). From the total capacity and porosity data, we could finally estimate that up to 80 % of the total porosity of the $DBP_{60}$ electrode (vs. less than 3 % for GDL) can be filled by $Li_2O_2$, nicely showing the very positive attribute of such interconnected multi-size porous domains as previously suggested by modeling and inspiration from other (e.g. living) systems.


## Acknowledgments

The authors would like to thank Dr. Benoît Fleutot and Dr. Mathieu Morcrette (LRCS) for helpful discussions. We deeply acknowledge Zodiac Aerospace, Safran and Airbus for their strong support on the IRT Saint-Exupéry CELIA project. Also, the authors are sincerely grateful to Dolores Hubert for her help on IR measurements.

**Bibliography**


1. Chmiola, J. *et al.* Anomalous Increase in Carbon Capacitance at Pore Sizes Less Than 1 Nanometer. *Science (80-. ).* **313,** 1760–1763 (2015).
2. El Hannach, M. *et al.* Characterization of pore network structure in catalyst layers of polymer electrolyte fuel cells. *J. Power Sources* **247,** 322–326 (2014).
3. Malek, K. & Franco, A. A. Microstructure-based modeling of aging mechanisms in catalyst layers of polymer electrolyte fuel cells. *J. Phys. Chem. B* **115,** 8088 (2011).
4. Xue, K.-H. H., Nguyen, T.-K. K. & Franco, A. A. Impact of the Cathode Microstructure on the Discharge Performance of Lithium Air Batteries: A Multiscale Model. *J. Electrochem. Soc.* **161,** E3028–E3035 (2014).
5. Gaya, C., Yin, Y., Torayev, A., Mammeri, Y. & Franco, A. A. Investigation of bi-porous electrodes for lithium oxygen batteries. *Electrochim. Acta* **279,** 118–127 (2018).
6. Radin, M. D. & Siegel, D. J. *Rechargeable Batteries*. (Springer International Publishing, 2015).
7. Williford, R. E. *et al.* Optimization of Air Electrode for Li/Air Batteries. *J. Electrochem. Soc.* **157,** A487–A492 (2010).
8. Sakai, K., Iwamura, S. & Mukai, S. R. Influence of the Porous Structure of the Cathode on the Discharge Capacity of Lithium-Air Batteries. *J. Electrochem. Soc.* **164,** A3075–A3080 (2017).
9. Gaillard, C., Despois, J. F. & Mortensen, A. Processing of NaCl powders of controlled size and shape for the microstructural tailoring of aluminium foams. *Mater. Sci. Eng. A* **374,** 250–262 (2004).
10. Elango, R., Demortière, A., De Andrade, V., Morcrette, M. & Seznec, V. Thick Binder-Free Electrodes for Li-Ion Battery Fabricated Using Templating Approach and Spark Plasma Sintering Reveals High Areal Capacity. *Adv. Energy Mater.* **8,** 1703031 (2018).
11. Tarascon, J. M., Gozdz, A. S., Schmutz, C., Shokoohi, F. & Warren, P. C. Performance of Bellcore's plastic rechargeable Li-ion batteries. *Solid State Ionics* **86–88,** 49–54 (1996).
12. Gozdz, A. S., Tarascon, J. M. & Schmutz, C. N. Rechargeable lithium intercalation battery hybrid polymeric electrolyte. (1994).
13. Gozdz, A. S., Schumtz, C. N., Tarascon, J. M. & Warren, P. C. Method of Making an Electrolyte activatable Lithium-ion Rechargeable Battery Cell. (1995).
14. Gozdz, A. S., Schumtz, C. N., Tarascon, J. M. & Warren, P. C. Lithium Secondary Battery Extraction Method. (1996).
15. Du Pasquier, A. *et al.* Plastic PVDF-HFP electrolyte laminates prepared by a phase-inversion process. *Solid State Ionics* **135,** 249–257 (2000).
16. Prosini, P. P., Villano, P. & Carewska, M. A novel intrinsically porous separator for self-standing lithium-ion batteries. *Electrochim. Acta* **48,** 227–233 (2002).
17. Richard, M. N., Koetschau, I. & Dahn, J. R. A Cell for In Situ X-Ray Diffraction Based on Coin Cell Hardware and Bellcore Plastic Electrode Technology. *J. Electrochem. Soc* **144,** 554–557 (1997).
18. Scrosati, B. & Garche, J. Lithium batteries: Status, prospects and future. *J. Power Sources* **195,** 2419–2430 (2010).
19. Tarascon, J. M. & Armand, M. Issues and challenges facing rechargeable lithium batteries. *Nature* **414,** 359–67 (2001).
20. Blyr, A., Sigala, C., Amatucci, G. & Tarascon, J. M. Self-Discharge of LMO/C Li-ion cells in their discharge state. *J. Electrochem. Soc.* **145,** (1998).

21. Morcrette, M. *et al.* In situ X-ray diffraction techniques as a powerful tool to study battery electrode materials. *Electrochim. Acta* **47,** 3137–3149 (2002).
22. Garza, L. L., Connor, P. A. & Torres-martõ, L. M. Investigation of lead tin fluorides as possible negative electrodes for Li-ion batteries. *J. Power Sources* **98,** 473–476 (2001).
23. Key, B. *et al.* Real-Time NMR Investigations of Structural Changes in Silicon Electrodes for Lithium-Ion Batteries. *J. Am. Chem. Soc.* **131,** 9239–9249 (2009).
24. Lu, Z., MacNeil, D.D. & Dahn, J.R. Layered Cathode Materials Li[$Ni_xLi(1/3-2x/3)Mn(2/3-x/3)$]$O_2$ for Lithium-Ions Battery. *Electrochem. Solid-State Lett.* **4,** A191 (2001)
25. MacNeil, D. D., Lu, Z., Chen, Z. & Dahn, J. R. A comparison of the electrode/electrolyte reaction at elevated temperatures for various Li-ion battery cathodes. *J. Power Sources* **108,** 8–14 (2002).
26. Laruelle, S. *et al.* X-ray absorption study of cobalt vanadates during cycling usable as negative electrode in lithium battery. *J. Power Sources* **97–98,** 251–253 (2001).
27. Poizot, P., Laruelle, S., Grugeon, S., Dupont, L. & Tarascon, J. M. Nano-sized transition-metal oxides as negative-electrode materials for lithium-ion batteries. **407,** (2000).
28. Fisher, R. a. *et al.* Recent advances in polyaniline composites with metals, metalloids and nonmetals. *Energy Environ. Sci.* **3,** 4889–4899 (2013).
29. Belliard, F. & Irvine, J. T. S. Electrochemical performance of ball-milled ZnO-SnO2 systems as anodes in lithium-ion battery. *J. Power Sources* **97–98,** 219–222 (2001).
30. Larcher, D. *et al.* Combined XRD, EXAFS, and Mössbauer Studies of the Reduction by Lithium of α-Fe2O3 with Various Particle Sizes. *J. Electrochem. Soc.* **150,** A1643 (2003).
31. Guy, D., Lestriez, B., Bouchet, R., Gaudefroy, V. & Guyomard, D. Improvement of lithium battery performance through composite electrode microstructure optimization. *Ionics (Kiel).* **10,** 443–449 (2004).
32. Guy, D., Lestriez, B., Bouchet, R., Gaudefroy, V. & Guyomard, D. Tailoring the Binder of Composite Electrode for Battery Performance Optimization. *Electrochem. Solid-State Lett.* **8,** A17 (2005).
33. Guy, D., Lestriez, B., Bouchet, R. & Guyomard, D. Critical Role of Polymeric Binders on the Electronic Transport Properties of Composites Electrode. *J. Electrochem. Soc.* **153,** A679 (2006).
34. Du Pasquier, A. *et al.* Mechanism for Limited 55 ° C Storage Performance of Li 1.05 Mn1.95O4 Electrodes. *J. Electrochem. Soc.* **146,** 428–436 (1999).
35. Du Pasquier, A. *et al.* Differential Scanning Calorimetry Study of the Reactivity of Carbon Anodes in Plastic Li-Ion Batteries. *J. Electrochem. Soc.* **145,** 472–477 (1998).
36. Barrett, E. P., Joyner, L. G. & Halenda, P. P. The Determination of Pore Volume and Area Distributions in Porous Substances. I. Computations from Nitrogen Isotherms. *J. Am. Chem. Soc.* **73,** 373–380 (1951).
37. Brunauer, S., Emmett, P. H. & Teller, E. Adsorption of Gases in Multimolecular Layers. *J. Am. Chem. Soc.* **60,** 309–319 (1938).
38. Ishak, H. *et al.* Aqueous solubility, vapor pressure and octanol-water partition coefficient of two phthalate isomers dibutyl phthalate and di-isobutyl phthalate contaminants of recycled food packages. *Fluid Phase Equilib.* **427,** 362–370 (2016).
39. David Linden & Thomas Reddy. Handbook of Batteries. in *Handbook of Batteries* (ed. Mc Graw Hill Professional) 74 (R. R. Donelley & Sons Coompany, 2001).
40. Griffith, L. D., Sleightholme, A. E. S., Mansfield, J. F., Siegel, D. J. & Monroe, C. W. Correlating $Li/O_2$ cell capacity and product morphology with discharge current. *ACS Appl. Mater. Interfaces* **7,** 7670–7678 (2015).